

Large-Scale Autonomous Gas Monitoring for Volcanic Environments: A Legged Robot on Mount Etna

Julia Richter¹ , Turcan Tuna¹ , Manthan Patel¹ , Takahiro Miki¹ , Devon Higgins² , James Fox² , Cesar Cadena¹ , Andres Diaz² , and Marco Hutter¹

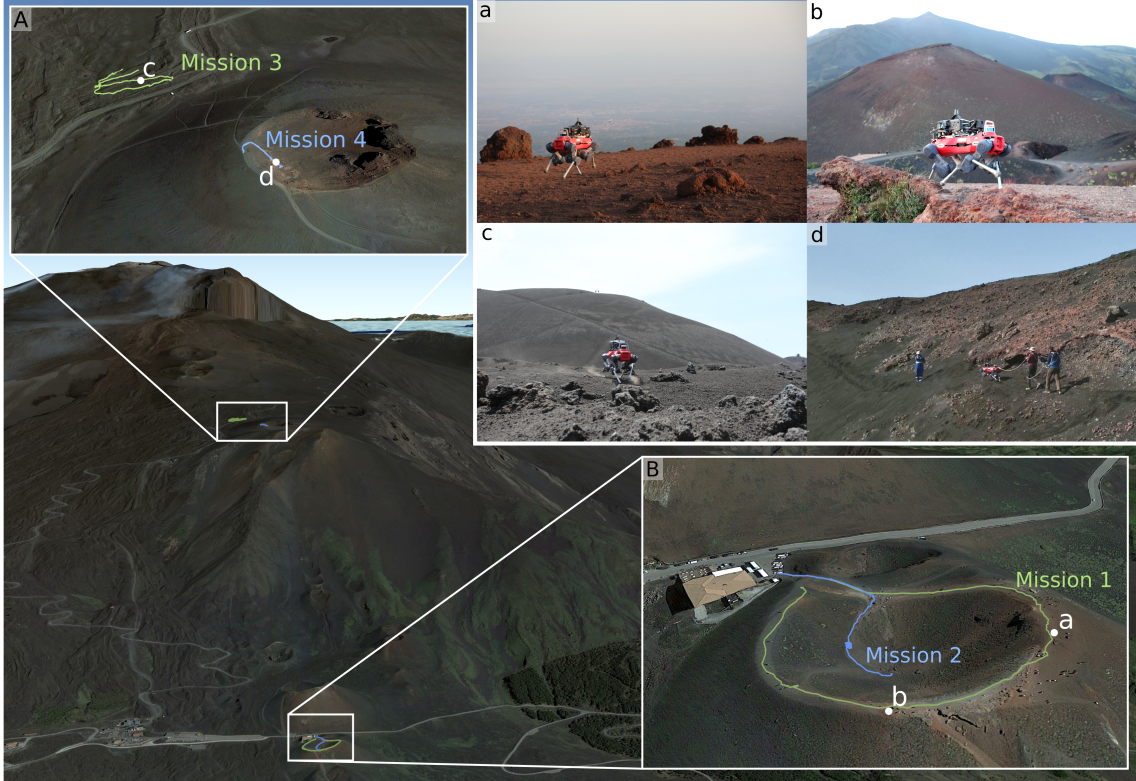


Fig. 1. Aerial overview of Mount Etna with the four completed missions indicated. (A-B) Zoomed views showing detailed trajectories of two mission areas. (a-c) Images from autonomous helium-mapping missions. (d) Image from the teleoperated mission measuring volcanic gases at an active crater.

Abstract—Volcanic gas emissions are key precursors of eruptive activity. Yet, obtaining accurate near-surface measurements remains hazardous and logistically challenging, motivating the need for autonomous solutions. Limited mobility in rough volcanic terrain has prevented wheeled systems from performing reliable *in situ* gas measurements, reducing their usefulness as sensing platforms. We present a legged robotic system for autonomous volcanic gas analysis, utilizing the quadruped ANYmal, equipped with a quadrupole mass spectrometer system. Our modular autonomy stack integrates a mission planning interface, global planner, localization framework, and terrain-aware local navigation. We evaluated the system on Mount Etna across three autonomous missions in varied terrain, achieving successful gas-source detections with autonomy rates of 93–100%. In addition, we conducted a teleoperated mission in which the robot measured natural fumaroles, detecting sulfur dioxide and carbon dioxide. We discuss lessons learned from the gas-analysis and autonomy perspectives, emphasizing the need for adaptive sensing strategies, tighter integration of global and local planning, and improved hardware design.

I. INTRODUCTION

About 29 million people live within 10 km of an active volcano [1], putting a substantial population at continued risk. Between 2010 and 2022, volcanic eruptions took the lives of more than a thousand people [2]. Scientists have been focusing on protecting affected populations through monitoring and analysis that enable timely warnings and evacuation. Monitoring is often conducted through the deployment of sensor networks that track ground deformation, seismic activity, and volcanic gas emissions. Eruptions are often preceded by changes in these signals on timescales from years to minutes, enabling forecasts of eruption timing [3]. These signals can be acquired remotely or *in situ*, where these different data collection schemes are complementary to each other [3]. This work focuses on autonomous *in situ* gas measurements, which enable the real-time estimation of volatile concentration and composition relevant to magmatic processes [4,5].

Conducting *in situ* gas measurements requires bringing instruments to fumaroles – small openings and fractures that

¹ Robotic Systems Lab (RSL), ETH Zürich, Zürich, Switzerland

² Intelligent Sensor Solutions, INFICON Inc., East Syracuse, NY, US

Supplementary video: https://youtu.be/7_a3BFefcJE

emit volcanic gases and steam and typically cluster near active vents. As a consequence, these sites are often hazardous due to unstable terrain, toxic gases (e.g., SO_2 , H_2S), and sudden explosive phreatic or pyroclastic eruptions, making human-assisted sampling particularly dangerous. Mobile robotic systems enable event-driven sampling in demanding and evolving volcanic environments. They can simultaneously acquire gas, thermal, and topographic data, providing essential context for interpretation [6]–[8]. Mobility offers four key advantages: (i) *adaptability* in a highly dynamic environment: fixed sensors can be destroyed by eruptions, overrun by lava or buried by tephra, or become irrelevant when degassing migrates, whereas a robot can reposition, search for new fumaroles, and track a shifting plume; (ii) *event-driven sampling*: the system can be dispatched rapidly to emergent activity (e.g., sudden degassing or eruptive phases) without redeploying personnel; (iii) *contextual sensing*: robots can co-acquire gas data with visual/spectral imagery, thermal measurements, and LiDAR-based topography, providing essential spatial and temporal context for interpreting fluxes and composition; and (iv) *spatial coverage*: a mobile sensor can survey large areas with a single instrument, making it feasible to deploy expensive, high-performance devices.

Prior work has leveraged unmanned aerial vehicles (UAVs) for plume sampling [6,7,9]. UAVs are effective for vent-level plumes because they can approach vent airspace while maintaining a safe standoff. Near-surface degassing, however, occurs at fumaroles distributed across the volcano with variable flux and composition (one example shown in Figure 7). Rapid dilution means that accurate sampling requires proximity to the source [4], which is particularly challenging for UAVs in complex terrain and unstable winds.

Different research groups have developed specialized unmanned ground vehicles (UGVs) to address the challenges of source-proximal plume measurements [8,10]. However, this also introduces locomotion and terrain hazards, such as loose tephra, steep slopes, lava ridges, and boulder fields [8]. Current wheeled and wheeled-legged rovers for volcanic monitoring have limited adaptability to uneven ground, compromising their stability. To protect sensitive instruments and avoid rollover, they must move slowly, which reduces operational efficiency and limits their practicality as in situ measurement platforms. Additionally, although several robotic systems have been developed for volcanic gas measurement, to the best of the authors' knowledge, none have conducted successful in situ measurements on an active volcano. The primary obstacle lies in the inaccessibility of fumaroles, which demand advanced locomotion capabilities and sufficient efficiency to reach remote sites. Moreover, current ground systems are primarily teleoperated; however, radio links can become intermittent during eruptions or in rugged terrain, making continuous teleoperation impractical and motivating the development of autonomous mission capabilities [11].

In recent years, legged robots have emerged as a new class of ground platforms capable of traversing diverse terrains. Their feasibility for in-the-wild applications has been demonstrated in missions ranging from teleoperated to partially autonomous operation. Teleoperated deployments are common

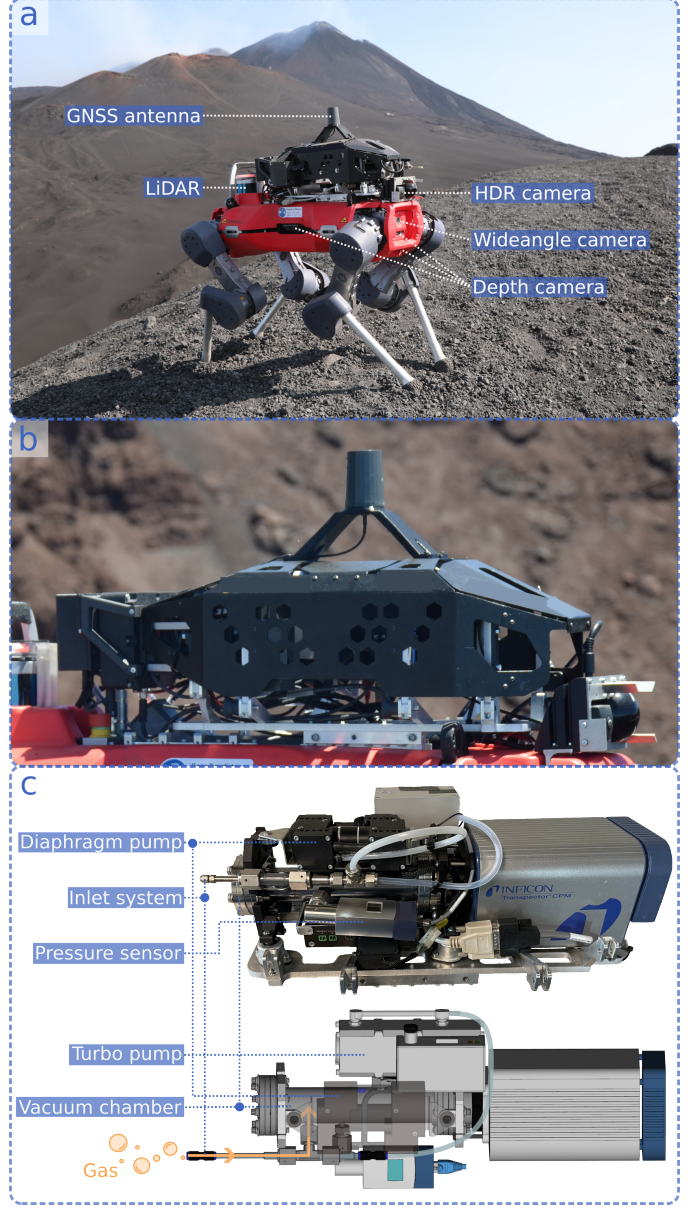


Fig. 2. Overview of the robotic system equipped with the gas-sensing payload and perception sensors. (a) Robot with labeled sensor components. (b) Gas-sensing payload with rollcage. (c) Transpector® MPH quadrupole mass spectrometer subsystem.

in wildlife observation [12] or soil sampling [13], whereas some initial approaches use partial autonomy, e.g., for planetary analog exploration [14] or forest inventory [15]. In many systems, the mission design remains human-in-the-loop: an operator specifies dense goals, such as a set of waypoints or a route, which defines sampling locations. The robot then navigates along these goals with local obstacle avoidance under safety supervision [13]–[15].

In this article, we present a legged robotic system for autonomous volcanic gas monitoring that integrates a mobile mass spectrometer with a high-level autonomy stack. We describe the hardware and software integration of the mass spectrometer, enabling precise in situ gas analysis during field operation. We introduce the methods developed for terrain-aware

navigation in extreme outdoor environments, allowing extended autonomous missions with minimal operator input. The proposed approach is validated through three autonomous field missions on Mount Etna, representing the first successful volcanic gas measurements performed by a ground robot in an active volcanic area. We further discuss key lessons learned from these real-world deployments, highlighting practical challenges and their implications for future autonomous systems for gas sensing and long-range navigation in natural environments. Ultimately, this work aims to support volcanologists in both regular and event-driven monitoring of active areas by enabling source-proximal gas measurements beyond the reach of human operators.

The rest of this paper is structured as follows. Section II describes the hardware and software architecture with its components. Section III presents the three autonomous missions we conducted at Mount Etna, while Section IV shows the results of the plume measurements we conducted. We discuss lessons learned in Section V and draw a conclusion in Section VI.

II. SYSTEM DESCRIPTION

A. Robotic Platform

Our robotic system consists of two parts, namely, the locomotion platform ANYmal, an off-the-shelf quadruped produced by ANYbotics AG, and a gas-sensing payload.

Each leg of the ANYmal has three actuated joints, enabling hip abduction/adduction, hip flexion/extension, and knee flexion/extension. The robot weighs 50 kg and has a payload capacity of 12 kg. It is powered by a 907 Wh lithium-ion battery and has, at maximum payload, a runtime of about 1 h.

As shown in Figure 2a, the robot is equipped with various sensors. It has six RealSense D435i depth cameras for close-range depth perception and a Velodyne VLP-16 LiDAR for long-range distance measurements, complemented by an IMU. The robot is further equipped with two wide-angle FLIR Blackfly RGB cameras. Additionally, we integrate a TIER IV C1 camera with a 198° field of view and High Dynamic Range (HDR) capabilities for enhanced visibility under variable lighting conditions. Moreover, the robot is equipped with a Global Navigation Satellite System (GNSS) receiver, specifically a Swift Navigation Piksi Multi, operating without Real-Time Kinematic (RTK) corrections. The onboard computation is handled by two internal Intel Core i7 processors, complemented by an NVIDIA Jetson Orin NX for additional GPU-accelerated processing, used, for example, in the Elevation Mapping module, explained in Section II-C3.

B. Scientific Gas-Sensing Payload

To analyze volcanic gases in situ, the sensing system must provide precise, selective, and robust measurements under harsh environmental conditions. Conventional approaches typically employ non-dispersive infrared (NDIR) sensors (e.g., for CO₂, CO, H₂O), electrochemical sensors (e.g., for SO₂, H₂S, HCl, HF), and semiconductor sensors (e.g., for H₂) [4]. While effective for targeted gas components, these sensors have a limited dynamic range, are prone to cross-sensitivity

and degradation in acidic volcanic environments [4]. To address these limitations, we employ a compact mass spectrometer as the primary sensing instrument, which has been previously validated in volcanic environments [16]. This analytical instrument identifies compounds based on their mass-to-charge ratio, providing high selectivity and accuracy across a wide range of gas components [5]. In practice, it can resolve characteristic atomic mass units (amu) of various compounds, such as Hydrogen (H₂, 2 amu), Helium (He, 4 amu), Carbon Dioxide (CO₂, 44 amu), and Sulfur Dioxide (SO₂, 64 amu), along with many other gases, isotopes, and molecular fragments. Moreover, its six-order-of-magnitude dynamic range prevents saturation at high concentrations, enabling reliable measurements both within dense fumarolic plumes and in downwind regions with sub-ppm (parts per million) concentrations.

The instrument we employ is an INFICON Transpector® MPH quadrupole mass spectrometer. To operate, it requires a high-vacuum environment, which is provided by a compact two-stage pumping setup consisting of a miniature diaphragm pump and a very small turbomolecular pump (Figure 2c). Ambient air enters the system through a stainless-steel capillary with a fixed flow restriction, which controls the gas flow into the measurement chamber. The diaphragm pump first lowers the pressure from atmospheric conditions to the medium-vacuum range (1×10^{-3} bar), after which the turbomolecular pump further reduces it to approximately 1×10^{-7} bar. At this pressure, the incoming gas is ionized by an electron beam, and the resulting ions are separated by their mass-to-charge ratio in the quadrupole analyzer, producing a spectrum that reveals the gas composition.

The used sensor has a mass range of 1 – 200 amu with a detection limit of <1 ppm in controlled environments and an acquisition time of 1.8 ms per mass data point. The response time is approximately 3 s, primarily determined by the inlet system, which consists of a 1 m capillary that reduces the difference between atmospheric and vacuum pressure levels.

The complete mass spectrometer subsystem weighs 8.7 kg. As shown in Figure 2b, we constructed an aluminium rollcage weighing approximately 3 kg to protect the instrument from fall damage. The mass spectrometer is powered through the robot's output port, with an average power consumption of 36 W, and communicates via TCP/IP through its native API.

C. Software Architecture

The software architecture, shown in Figure 3, follows a modular design structured into two main categories. **Blue** denotes the navigation modules, responsible for global and local path planning and for executing velocity commands through the locomotion controller. **Green** indicates the perception modules, which process data from multiple onboard sensors to perform state estimation and elevation mapping. Together, these components enable the hierarchical planning and control pipeline described below, which orchestrates the robot's autonomous behavior from high-level mission specification down to low-level actuation. At the highest level, a *Mission Planning* Graphical User Interface (GUI) allows the *Operator* to define mission **targets**, which serve as targets for

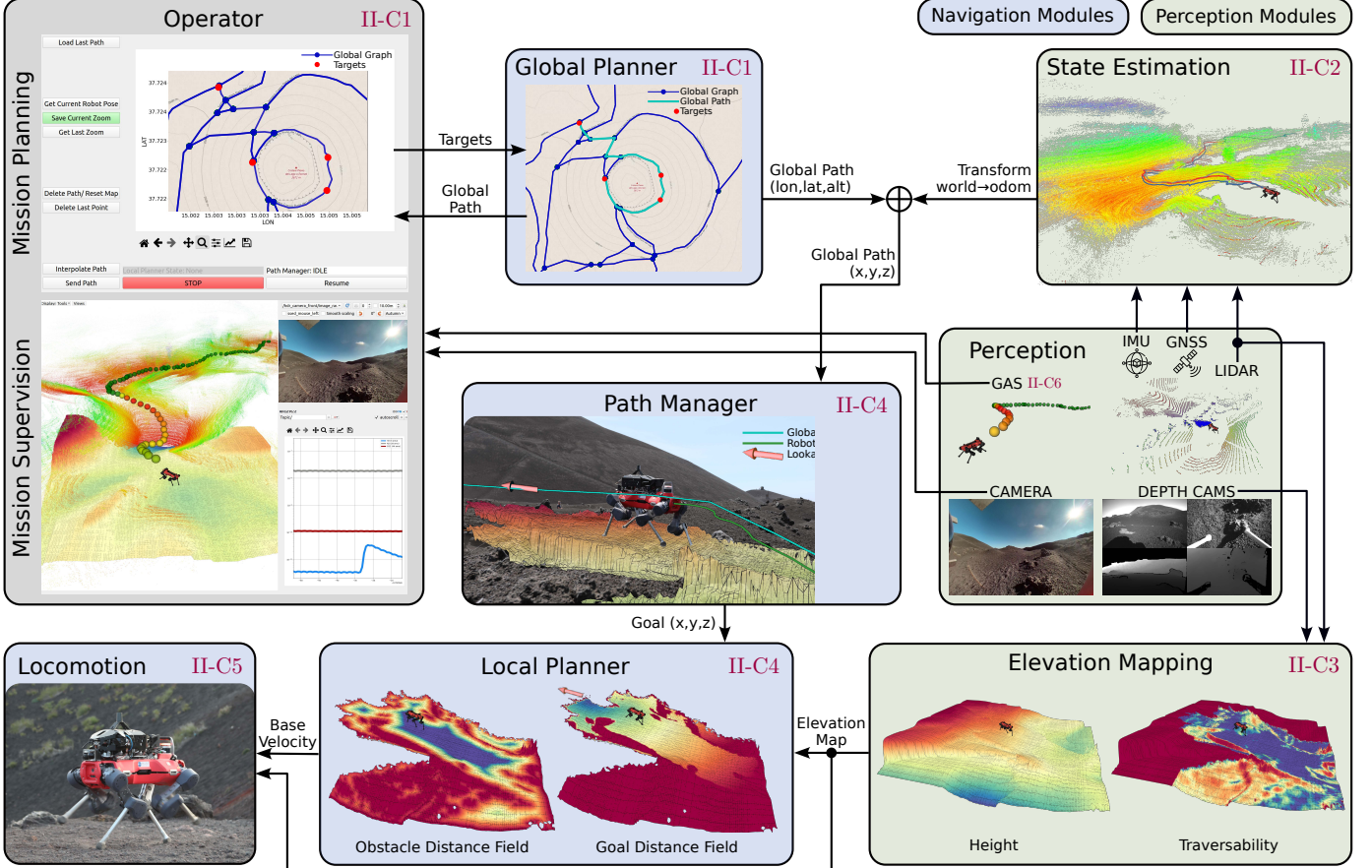


Fig. 3. Overview of software architecture. The architecture is organized into two main parts: the blue navigation modules, responsible for global and local path planning and locomotion control, and the green perception modules, which handle state estimation and elevation mapping. Information flows from high-level mission planning (top left) to low-level actuation (bottom left), while feedback from perception enables autonomous operation and live supervision of mapping and gas measurements. The numbers in pink correspond to the sections of this paper in which the respective modules are described.

the *Global Planner* to generate a global path. Since this path is represented in geographic coordinates (longitude, latitude, and altitude), it is transformed into the robot's local reference frame through sensor fusion of global GNSS data with point-cloud Simultaneous Localization and Mapping (SLAM) and kinematic measurements. From the transformed path, a *lookahead waypoint* is sampled and passed to the *Local Planner*. The *Local Planner* then computes a feasible local trajectory toward the *lookahead waypoint* based on the height and traversability information provided by the *Elevation Mapping* module. Finally, the resulting base velocity commands are executed by a reinforcement-learning (RL) *Locomotion* controller that drives the individual leg actuators to achieve the desired body motion. During the mission, the operator can monitor the system through the *Mission Supervision* interface, which provides access to the assembled SLAM map, live camera feeds, and real-time gas measurement data.

1) Mission Planning: The mission planning GUI displays globally referenced satellite data in longitude-latitude coordinates, enabling intuitive image-based target selection. The purpose of the image is to provide the operator with sufficient environmental context for planning, ideally based on high-resolution satellite imagery. Since this data is not universally available, we base the visualization on the Tracestrack

Topo layer of OpenStreetMap¹, which includes path networks, types, and dense contour lines that allow recognizing topographic features such as craters. The data are retrieved via the OpenStreetMap API, and an example is shown in Figure 3 (Global Planner). For deployments where this visualization is insufficient, the interface also allows importing aerial imagery captured by a drone as a substitute for high-resolution satellite data.

Global missions are planned interactively by placing targets on the GUI according to the mission objectives. The global planner then interpolates a path between these targets. Specifically, we employ an A* planner operating on a road network graph generated offline using the OpenStreetMap Python wrapper OSMnx [17], visualized in blue in Figure 3 (Global Planner). Targets located outside the graph are linearly connected to their nearest projection point. The A* cost between two connected nodes is defined as the Euclidean distance. Although slope and surface characteristics naturally influence traversal cost, publicly available digital elevation models have coarse resolutions (10 – 30 m), making it difficult to estimate these factors a priori.

¹<https://www.openstreetmap.org/#layers=P>

As shown in Figure 3, the mission planning GUI is operated directly by the user and outputs a global path in longitude-latitude-altitude coordinates, which is transformed into the Cartesian robot frame based on the state estimation described in the following section.

2) State Estimation: Accurate state estimation, including a reliable world-referenced robot pose, is a prerequisite for executing long-range and large-scale navigation tasks. We build on the optimization-based multi-sensor fusion framework Holistic Fusion (HF) [18] and adapt it to better handle the challenges of long-range deployments, such as numerical ill-conditioning, intermittent and sometimes unreliable GNSS, and inconsistent estimates that drift over time. It fuses three complementary sources: *i*) globally referenced but noisy non-RTK GNSS measurements, *ii*) globally consistent but drifting Light Detection and Ranging (LiDAR)-SLAM poses, and *iii*) short-term stable inertial-kinematic odometry from ANYbotics' internal kinematic-inertial estimator. For LiDAR-SLAM poses, we employ the field-tested degeneracy-aware X-ICP [19] LiDAR-based SLAM framework. This module provides smooth, temporally consistent SE(3) pose estimates (i.e., full 6-DoF position and orientation) of the robot within the evolving LiDAR map. While LiDAR-SLAM solutions are designed for temporally consistent performance, their accuracy ultimately depends on the quality of the incoming LiDAR data. Under nominal conditions, the sensor provides sufficient geometric structure for reliable scan matching. In environments with loose soil, however, foot slip induces high dynamics in the robot, which in turn introduces motion distortions into the LiDAR observations. Combined with the already sparse geometric structure typical of volcanic terrain, these distortions can cause LiDAR-SLAM to drift over long distances. Therefore, in order to achieve globally consistent localization, the LiDAR-SLAM estimates must be fused with GNSS signals. The resulting estimator remains stable during GNSS outages, and quickly re-anchors to the global frame once absolute information is restored.

HF formulates estimation as a factor-graph Maximum a Posteriori (MAP) problem,

$$\mathcal{X}^* = \arg \max_{\mathcal{X}} p(\mathcal{X} | \mathcal{Z}) \propto p(\mathcal{Z} | \mathcal{X}) p(\mathcal{X}), \quad (1)$$

where \mathcal{Z} collects all sensor data and priors, and \mathcal{X} comprises robot and alignment variables $\mathcal{X} = \{ {}^I \mathcal{X}_{N_I}, {}^G \mathcal{X}_{N_G}, {}^R \mathcal{X}_{N_R} \}$. Here, ${}^I \mathcal{X}_{N_I}$ denotes the time-indexed robot state in the world frame, while ${}^G \mathcal{X}_{N_G}$ and ${}^R \mathcal{X}_{N_R}$ parameterize the global and reference-frame alignments that couple local mapping with the global reference frame.

We make two central design choices in order to enhance HF and make it more robust for long-distance deployment. First, instead of treating the LiDAR-SLAM output as incremental odometry, we introduce *absolute* LiDAR-SLAM pose factors into the graph. Second, we explicitly estimate the alignment between the evolving LiDAR-SLAM map and the world frame as part of the optimization. Concretely, the alignment state in ${}^R \mathcal{X}_{N_R}$ at time k between the world frame W and the Open3D map frame M_{o3d} is

$$T_{W M_{o3d}} \in \text{SE}(3). \quad (2)$$

This variable anchors LiDAR-SLAM poses to the global estimate on the fly, enabling the fusion to (a) maintain smooth, globally consistent trajectories across GNSS dropouts, (b) query the robot state directly in the map frame at any time, and (c) model uncertainty growth according to the assumed drift characteristics of the mapping back end (rather than just local registration noise). Together, the degeneracy-aware LiDAR SLAM and the alignment-aware HF fusion yield accurate global localization and reliable local consistency across long, geometry-poor traverses.

Figure 3 illustrates how the *State Estimation* module interfaces with the navigation stack. Its main task is to localize the robot in the world frame W and provide a transform to the global path, defined in the geographic frame LLA, into a local Cartesian representation usable by the *Local Planner*. For this, we construct a Cartesian East-North-Up (ENU) frame anchored at the robot's initial geographic position, and compute LLA \rightarrow ENU on the WGS-84 ellipsoid. We additionally employ a geoid undulation model (EGM2008) to convert the ellipsoidal heights to orthometric heights referenced to mean sea level, thereby enhancing the accuracy of the transformation. The global Cartesian frame ENU has a fixed transform to the earlier introduced world frame W , ensuring consistent alignment between global coordinates and local navigation tasks.

3) Elevation Mapping and Traversability Estimation: Navigating in unstructured environments requires a reliable spatial representation of the surrounding terrain. 2.5D elevation maps provide a memory-efficient solution for ground robots, supporting multimodal sensor fusion and compatibility with various downstream tasks. In this representation, each grid cell encodes the local terrain height, and additional layers can store complementary information such as traversability. Such maps are essential for both perceptive locomotion, by identifying safe foothold regions, and navigation planning, by enabling the computation of feasible paths that avoid high-risk areas. We employ *Elevation Mapping CuPy* [20], an elevation mapping framework accelerated on the GPU for fast and efficient fusion of multi-modal sensory inputs. As shown in Figure 3, it integrates depth data from six RGB-D cameras with measurements from the LiDAR to construct an ego-centric elevation map of size 12 m \times 12 m at a resolution of 0.06 m. For geometric traversability estimation, we follow the approach of [21] and use a lightweight convolutional neural network trained on a small set of manually annotated terrain samples to predict a traversability score between 0 and 1. To improve the spatial consistency of the predictions and increase safety margins in rough terrain, we further refine the traversability layer through *inpainting* and *dilation* operations with a kernel size of 0.24 m. Examples of the resulting maps are shown in Figure 3 (*Elevation Mapping*). The two generated layers, *Height* and *Traversability*, are subsequently used by the *Local Planner*, described in the following section.

4) Local Navigation: While the global planner computes a feasible high-level path, local uncertainties, such as GNSS drift or previously unseen obstacles, increase the demand for a reactive local planner to follow this path safely. Since local planners optimize paths primarily within the robot's field of view, we introduce an intermediate *lookahead waypoint*,

visualised in Figure 3 (*Path Manager*), which is updated at 0.5 Hz, to guide the robot along the global path. The choice of lookahead distance critically influences how well the robot anticipates upcoming path geometry: if it is too large, especially around corners, the robot may deviate prematurely and enter local minima; if it is too small, the robot becomes overly sensitive to minor irregularities of the global path, such as local artifacts or offsets. To balance these effects, we dynamically adjust the lookahead distance according to the curvature of the global path: using a longer lookahead in straight, open areas to ensure stability, and a shorter lookahead in tight turns to maintain adherence to the intended route.

The path curvature at the robot's current position is obtained through the calculation outlined below and visualized in Figure 4. We first project the robot's position \mathbf{x}_{robot} onto the path to obtain the closest anchor point \mathbf{x}_i at index i . Two secant vectors $\mathbf{v}_i^{(p)}$ and $\mathbf{v}_i^{(n)}$ are then constructed, pointing forward and backward along the path from the anchor. Their normalized directions $\hat{\mathbf{v}}_i^{(p)}$ and $\hat{\mathbf{v}}_i^{(n)}$ define the local curvature κ_i via

$$\kappa_i = \frac{\theta_i}{\|\hat{\mathbf{v}}_i^{(n)}\|}, \quad \text{with } \theta_i = \arccos(\hat{\mathbf{v}}_i^{(p)} \cdot \hat{\mathbf{v}}_i^{(n)}), \quad (3)$$

where θ_i is the angular difference between the two vectors. The adaptive lookahead distance is then defined as

$$L(\kappa_i) = L_{\min} + \frac{L_{\max} - L_{\min}}{1 + |\kappa_i|/\kappa_{\text{ref}}}, \quad (4)$$

where L_{\min} and L_{\max} denote the min-max lookahead distances, and κ_{ref} controls sensitivity to curvature changes. Given the lookahead distance $L(\kappa_i)$ and the sampling interval Δs , we place $N(\kappa_i) = L(\kappa_i)/\Delta s$ samples along the path ahead of the anchor point. The final lookahead waypoint \mathbf{x}_{goal} is then obtained as an exponentially weighted average of these $N(\kappa_i)$ samples with respect to their arc-length distance from the anchor. This places stronger emphasis on the nearby path geometry while accounting for the structure of the upcoming trajectory. Figure 4 illustrates two examples of this procedure.

To follow this lookahead waypoint, we employ the *Field Local Planner* introduced by [22], which combines multiple vector fields using Riemannian Motion Policies (RMPs) for continuous obstacle avoidance and goal attraction. For obstacle avoidance, a Signed Distance Field (SDF) is used, which generates a repulsive field that drives the robot away from obstacles. It is constructed from the traversability map by thresholding it at 0.2 to mark obstacles, followed by computing and normalizing the Euclidean distance of each cell to the nearest obstacle. The goal attraction is implemented as a Geodesic Distance Field (GDF), which produces an attractive field that guides the local planner toward the goal. It is defined as a smooth scalar field over the traversable region, where each cell encodes the shortest-cost distance to the goal such that gradient descent over the field yields efficient local trajectories. Examples of both fields are shown in Figure 3 (*Local Planner*).

5) Locomotion Controller: Locomotion is a key component of the autonomy framework, ensuring that high-level planning and sensing objectives can be executed reliably in rough volcanic terrain. Our RL-based controller receives base velocity commands from the *Local Planner* and integrates

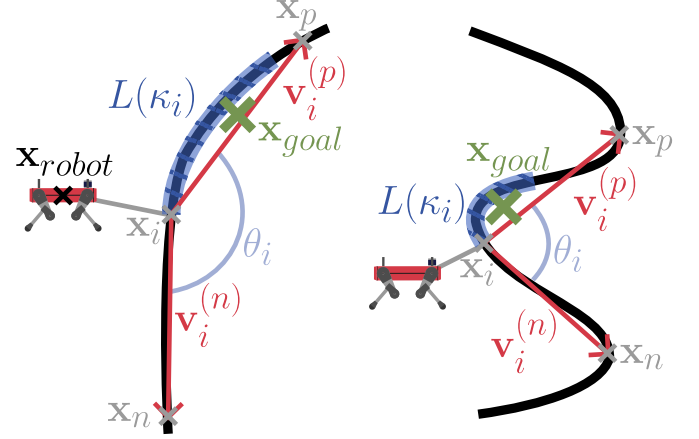


Fig. 4. Computation of curvature-based adaptive lookahead. The robot's position (\mathbf{x}_{robot}) is projected onto the path to obtain the nearest anchor point (\mathbf{x}_i), from which forward and backward secant vectors ($\mathbf{v}_i^{(p)}, \mathbf{v}_i^{(n)}$) define the local curvature (κ_i). The lookahead waypoint (\mathbf{x}_{goal}) is then placed based on curvature-dependent lookahead distance ($L(\kappa_i)$).

elevation-map information for perceptive locomotion, generating coordinated leg motions that maintain stability and energy efficiency on uneven terrain. Following the methodology of [23], the controller is trained entirely in simulation using a teacher-student distillation pipeline to enhance robustness in unstructured environments. A *teacher* policy is first trained with access to privileged information such as ground-truth terrain friction, additional payload mass, and external forces. Subsequently, a *student* policy learns to mimic the teacher's behavior without access to these privileged inputs. This setup encourages the student to implicitly estimate hidden physical parameters, yielding strong adaptability to variations in terrain and robot dynamics, such as changes in base mass or contact properties.

While a general policy trained with standard domain randomization can tolerate moderate payload changes, it exhibits less efficient gaits under significantly increased weight and shifted center of mass. To improve stability and efficiency, we trained an extended policy using payload-specific domain randomization. During training, the simulated robot's base mass was augmented to include the payload, and its center of mass was randomly varied within a plausible range to account for the uncertainty of the real instrument and rollcage. This payload information was provided to the teacher policy as a privileged input, enabling it to develop locomotion strategies specifically adapted to the altered dynamics. The resulting student policy retained this robustness while remaining fully deployable without privileged sensing. In practice, this approach produced a stable, terrain-adaptive gait that maintained reliable performance throughout the field campaign. Although the learned policy supports walking speeds of up to 1.5 m s^{-1} and slope climbing up to 25° , a conservative limit of 0.8 m s^{-1} was imposed during field operation for safety.

6) Gas Sensing and Data Processing: We developed a dedicated ROS package to interface directly with the mass spectrometer via its native API, enabling full control and real-time data acquisition on board the robot. The instrument

TABLE I
PERFORMANCE METRICS FOR THREE AUTONOMOUS MISSIONS.

Unit	Length m	Duration mm:ss	Gas sources detected	Interventions	Total intervention time mm:ss	RAD	AR %
Mission 1	388	10:02	3/5	4	0:43	0.0887	92.8
Mission 2	250	07:29	1/1	0	0:00	0	100
Mission 3	270	09:56	1/2	3	0:22	0.0490	96.3
Average	303	09:09	5/8	2.3	0:22	0.0459	96.4

supports two measurement modes: a *bin* scan, which repeatedly measures a predefined set of selected atomic mass values (e.g., [2, 4, 8, 44] amu), and an *analog* scan, which continuously records spectra over a specified range (e.g., 1-50 amu). We employ the *bin* mode for its higher sampling rate, which enables temporal mapping of gas concentrations during motion.

Through the ROS integration, all spectrometer measurements are automatically time-synchronized with the robot. This allows each gas sample to be globally and locally referenced, and visualized in the mission planning interface as colored markers along the robot's trajectory (Figure 5 *Gas*). The concentration levels are also plotted in real-time, providing the operator with immediate feedback for situational awareness and plume analysis.

III. AUTONOMOUS MISSIONS

A. Testing Setup

To evaluate the performance of the proposed system, field experiments were conducted on Mount Etna, Sicily, Italy. Mount Etna is one of the most active volcanoes in the world, offering diverse terrains that range from solidified lava flows to loose volcanic deserts. Its frequent degassing activity and well-developed road network enable safe yet realistic testing of robotic systems in a volcanic environment.

Several potential test sites were assessed on the mountain, prioritizing locations with a high likelihood of degassing activity. The main craters were excluded because they required a 2.5 km hike with an altitude gain of about 400 m from the nearest parking area, making access logistically infeasible. The next accessible location, the Barbagallo craters, was also unsuitable due to heavy tourist activity along a narrow path, which posed safety risks. Of the remaining accessible sites, the one where we observed active degassing during our campaign was the Laghetto crater, reachable via an unpaved road followed by a short walk and a steep ascent. However, the path leading to the fumaroles was narrow, steep, and covered in loose sand, as shown in Figure 7. Given these challenging conditions, the corresponding gas-measurement mission was conducted in teleoperated mode to ensure safety, with results discussed in Section IV.

The autonomy tests were instead performed at locations that provided safe conditions for autonomous navigation, where artificial gas sources were deployed to evaluate sensing performance. We designed three representative scenarios that reflect

typical challenges for autonomous operation on a volcano, distributed across different regions of Mount Etna, as shown in the region overview in Figure 1. Mission 1 (Figure 5-M1) followed the rim of the Silvestri crater, featuring a long traverse with few visual landmarks for localization. Mission 2 (Figure 5-M2) descended into the same crater, posing locomotion challenges due to steep slopes and a floor covered in rocks of different sizes. Mission 3 (Figure 5-M3) took place in a volcanic desert near the Laghetto crater, where fine sand and degraded GNSS reception made both locomotion and localization difficult. Navigation was further challenged by numerous rocks, irregular and loose terrain with slopes, and visually uniform but mechanically inconsistent sand, which made traversability difficult to predict during planning. During operation, data were streamed to the operator's computer for monitoring (Figure 3 *Mission Supervision*), while the operator remained at a safe distance to allow for safety-critical intervention. To demonstrate the gas-sensing capability in a controlled yet representative way, we placed helium bottles along the planned trajectories. Helium was selected because it is non-toxic, non-flammable, chemically inert, poses no environmental risk, and is easily detectable due to its negligible natural background concentration in the atmosphere. Results of the autonomous missions are presented below.

B. Autonomous Mission Results

The three autonomous missions were analyzed with respect to both gas-sensing performance and autonomous navigation reliability. Table I summarizes the deployment results. Two categories of performance measures were considered. First, gas-source detection was assessed by verifying, through post-mission analysis, whether the deployed sources were successfully identified in the recorded concentration data. Second, autonomy was quantified using two complementary metrics. The Robot Attention Demand (RAD) [24] was computed as

$$RAD = \frac{IE}{IE + NT}, \quad (5)$$

where the interaction effort (IE) denotes the average duration of operator interventions and the neglect tolerance (NT) represents the time intervals between them. The Autonomy Rate (AR) expresses the fraction of the total mission time during which the robot operated without human input, calculated as

$$AR = 100 \times \left(1 - \frac{T_{\text{intervention}}}{T_{\text{total}}} \right). \quad (6)$$

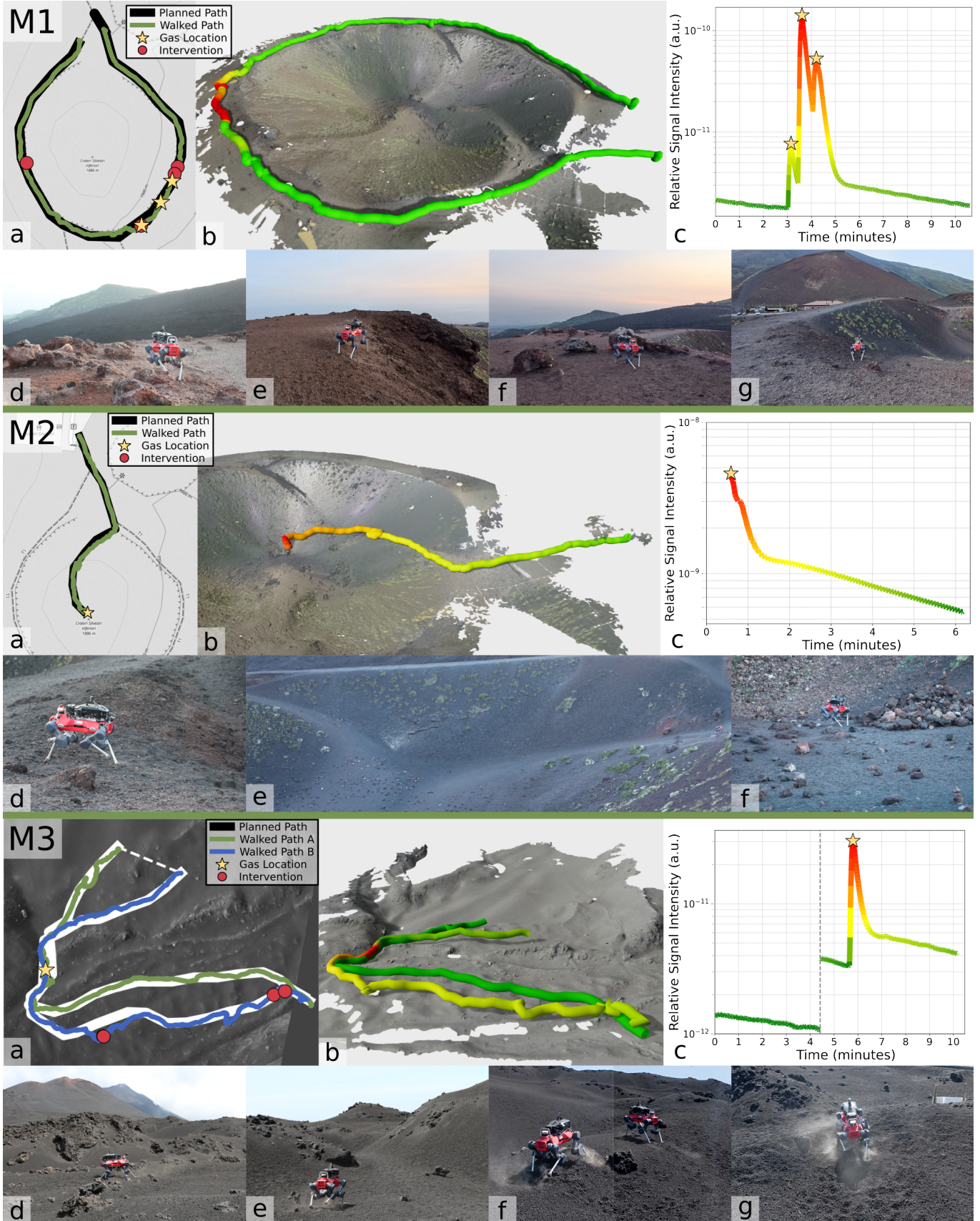


Fig. 5. Results of the three autonomous field missions on Mount Etna: M1-Crater Rim, M2-Crater Descent, and M3-Volcanic Desert. For each mission: (a) Satellite image showing the mission area with marked **Interventions** and detected **gas source locations**. (b) Terrain mesh with the traversed path, color-coded by relative gas concentration. (c) Time series of gas measurements using the same color map. (d-g) Representative images illustrating the robot's operation in varying terrain conditions.

All three missions were completed successfully, achieving RAD values below 0.1 and autonomy rates above 90%. Mission 2 was executed entirely autonomously, requiring no operator intervention, whereas Missions 1 and 3 involved short interventions to ensure equipment safety. The gas-source detection performance was affected by environmental conditions, resulting in five successful detections out of the eight deployed sources. In particular, average winds of 5 km h^{-1} and gusts up to 39 km h^{-1} , according to meteorological reports for the test days, led to plume dispersion and increased sensitivity to source placement.

Mission 1 – Crater Rim: The first experiment was conducted along the rim of the Silvestri crater. As shown in Figure 5 (M1d-M1g), the path had low-gradient slopes at the edges and several larger boulders distributed along the route (M1d, M1f). Figure 5 (M1b) shows the full trajectory projected onto a high-resolution mesh that we independently recorded using a Leica Geosystems RTC360 stationary scanner for visualization purposes. The corresponding time series is presented in Figure 5 (M1c). Out of the five helium sources deployed, the robot detected three at the correct locations, visible as clear peaks in the recorded signal. Due to the wind along the crater rim, the remaining two sources were not detected, as the gas plumes were blown away from the robot. For the identified detections, the time series in Figure 5 (M1c) shows a steep rising edge and a slower decay, which is typical for mass spectrometers due to residual gas remaining in the vacuum chamber after exposure.

Four operator interventions were required during this mission, as indicated in Figure 5 (M1e-M1g). One occurred when the local planner overestimated the space between two obstacles (M1f), two were caused by incorrect traversability estimation on fine ash (M1e), and one happened when the robot took a wrong turn toward unsafe terrain (M1g) due to subtle misalignment of the robot heading in the world frame. These interventions occurred in sections where the transformed global path deviated several meters from the real trail, as illustrated in two examples in Figure 6. The offset was caused by a combination of two factors. First, the limited positional accuracy of the OpenStreetMap data used for global path generation resulted in the planned path being shifted relative to its actual location. Second, the terrain of the crater rim contains weakly structured areas, in which point-cloud SLAM intermittently drifted since scan matching became poorly constrained and small registration errors accumulated. This effect was further amplified by GNSS position uncertainty of approximately $\pm 2 - 3 \text{ m}$. Because global orientation observability relies on both reliable SLAM geometry and an accurate GNSS position anchor, the simultaneous degradation of these two sources caused the fusion system to misinterpret small positional inconsistencies as changes in orientation, producing a rotational offset in the projected global path. As a result of these two factors, the lookahead waypoints were physically unreachable, leading the local planner to generate commands that steered the robot into local minima or low-traversability regions.

Mission 2 – Crater Descent: The second experiment started from approximately the same location as Mission 1, but this time the robot descended into the crater and returned

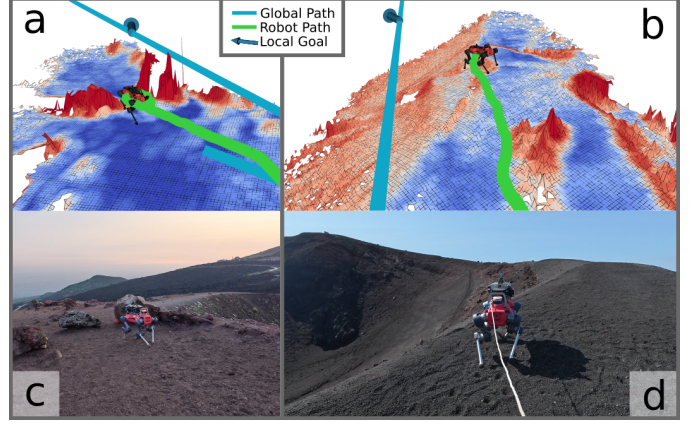


Fig. 6. Example of global-local path misalignment during an autonomous mission. (a,b) Mission GUI showing the [global path](#), the traversable trail (blue regions in the elevation map), and the robot's [past trajectory](#). (c,d) Corresponding camera view of the same scenes.

to the rim, as shown in Figure 5 (M2b). The path was moderately steep with partially loose ground, and the crater floor consisted of a boulder field with small to medium-sized rocks (Figure 5 (M2f)), both posing notable locomotion challenges.

The robot successfully descended into and exited the crater without any human intervention. The executed trajectory is shown in Figure 5 (M2a). As expected, the main challenge arose from the rocks on the crater floor. The elevation map struggled to capture these smaller obstacles, so the perceptual controller could not account for them. Consequently, the robot occasionally stepped on loose rocks that shifted under its weight, but the locomotion controller proved sufficiently robust to recover.

A single helium source was placed at the center of the crater. To illustrate a case where gas measurements are taken only in regions of expected degassing, the mass spectrometer was only activated once the target area was reached. The resulting gas concentrations measured during the exit from the crater are shown in the concentration map in Figure 5 (M2b). The time series data in Figure 5 (M2c) show a clear concentration peak, indicating that the robot successfully detected the gas source.

Mission 3 – Volcanic Desert: For this experiment, the robot traversed a volcanic desert near the Laghetto crater. As shown in Figure 5 (M3d-M3g), the terrain was hilly, with slopes of varying steepness and regions of differing sand density. Scattered throughout the area were sharp volcanic boulders of various sizes. A particular challenge in this mission was the traversal of a narrow valley (Figure 5 (M3e)).

The mission was planned from a road to a target location in the center of the field and back, as shown in Figure 5 (M3a) in [green](#) and [blue](#), respectively. A long hill between the start and goal required the global path to be routed around it, as the local planner could not account for an obstacle of that scale. Three operator interventions were required during the mission. The first intervention occurred when the locomotion controller failed to recognize a small hole next to a rock and did not lift its foot high enough to clear it, causing repeated collisions with the obstacle. For the other two interventions, the operator had to manually steer the robot because the local planner's

velocity commands, although correctly oriented, did not generate enough forward velocity to overcome slipping in fine sand uphill. One example is shown in Figure 5 (M3g). Figure 5 (M3f) shows another incident, where the robot failed to climb on the left side of a rock but succeeded on the right during the second attempt, highlighting how identical slopes and appearances can mask different soil behaviors. One challenge for localization occurred in the narrow valley, where the surrounding terrain further degraded GNSS reception and increased the uncertainty to approximately ± 6 m from the nominal $\pm 2 - 3$ m. Despite the reduced signal quality, the consistent local frame provided by the SLAM system helped the fusion-based localization maintain a stable global pose estimate and prevent deviation with respect to the target global robot position. While the synergetic effect of GNSS and point-cloud SLAM mitigated the issue, more reliable and environment-invariant sensing modalities should be investigated to prevent such cases.

A helium source was placed inside the valley, shown as a star in Figure 5 (M3a). The robot did not detect the gas on its first pass, likely because the plume was dispersed by the wind away from the inlet, but it successfully measured it during the return traversal, as shown in the time series in Figure 5 (M3c). In this plot, the grey line indicates a measurement pause, during which the operator temporarily halted data collection and repositioned the robot to better analyze the surroundings.

Overall, these field trials show that fully autonomous volcanic exploration with integrated gas sensing is feasible and effective, with robust system performance across diverse terrains. However, the performance is strongly coupled to environmental conditions. The experiments demonstrated how wind-driven plume dispersion significantly impacts gas detection reliability, underscoring the importance of perception and planning modules that actively consider wind dynamics and plume movement. At the same time, the operator interventions revealed key limitations in autonomy: imperfect global-to-local path alignment, uncertainty in terrain traversability, and partial observability in visually uniform landscapes. These aspects are discussed in more detail in Section V.

IV. VOLCANIC PLUME MEASURING

We conducted one teleoperated test near active fumaroles inside the Laghetto crater on Mount Etna. These fumaroles were located on a side slope with very loose ground, as shown in Figure 7a-f. The path leading to the plumes was narrow and ran nearly parallel to the contour lines with a subtle inclination with respect to the horizontal ground. While the central foot trail consisted of compacted soil, the surrounding areas were covered with loose, deep sand. Autonomous operation was infeasible, as even small lateral steps caused the robot's feet to sink deeply into the substrate (Figure 7f). The teleoperated mission took place under moderate wind conditions, which caused plume dilution and made gas measurements challenging, as the plume shifted rapidly around the robot. We monitored water vapor (H_2O , 18 amu), hydrogen sulfide (H_2S , 34 amu), carbon dioxide (CO_2 , 44 amu), and sulfur dioxide (SO_2 , 64 amu) as key volcanic volatiles, and nitrogen (N_2 , 28 amu) as a background reference. The robot was

commanded to move along the slope, occasionally stopping in areas where water vapor was visible.

Figure 7k visualizes the measurement site and the robot's trajectory, while Figure 7h shows the recorded gas concentrations over time. A distinct peak in sulfur dioxide is visible, corresponding to the time when the robot was directly adjacent to the fumarole. A smaller rise in sulfur dioxide and carbon dioxide was detected when the robot turned around and started its return. In contrast, no clear increase in water vapor concentration was observed, likely because of the already high ambient humidity levels, which made plume-related variations difficult to distinguish.

To validate the gas measurements obtained with the on-board mass spectrometer, we collected measurements manually using a miniGAS instrument (INFICON Hapsite® Scout), which combines GNSS data, temperature, pressure, and relative humidity with multiple electrochemical sensors, including those for CO_2 and SO_2 . The handheld instrument was carried along the same path and positioned in visible plumes to obtain reference readings. Figure 7i shows the corresponding CO_2 measurements plotted at the recorded locations, confirming the same fumarole positions as observed in Figure 7k. While the miniGAS SO_2 sensor did not register a clear signal, the robot-mounted mass spectrometer successfully detected a pronounced sulfur dioxide peak from approximately 0.5 m away. Conversely, the stronger CO_2 response of the handheld sensor can be attributed to its direct proximity to the emission source. Together, these results confirm the consistency between both sensing methods and support the reliability of the robot-mounted mass spectrometer for in situ volcanic gas analysis.

V. LESSONS LEARNED

A. Volcanic Gas Analysis

The robot successfully traversed the volcanic terrain in order to reach active fumaroles and conducted gas measurements, detecting distinct gas compositions from different plumes. However, the real-world deployment also revealed several practical challenges that are important to consider for the future. First, volcanic gas plumes are highly transient, particularly under strong wind conditions. Even with a fast and sensitive instrument such as the mass spectrometer, plume dispersion occasionally prevented accurate detection. This highlights the need for measurement strategies that better account for environmental conditions, such as incorporating visual gas-source detection or wind sensing for plume prediction. Second, for ground-level gases at low concentrations, the current inlet setup, mounted approximately 0.75 m above the ground, may be too high to effectively sample the plume. Future solutions would benefit from a deployable inlet mechanism capable of positioning the sampling point directly at or near the emission source.

B. Autonomy and Mobility

The autonomous missions demonstrated that reliable navigation on volcanic terrain is feasible, with autonomy rates exceeding 90%. Across three distinct environments – crater rim, crater descent, and volcanic desert – the robot consistently

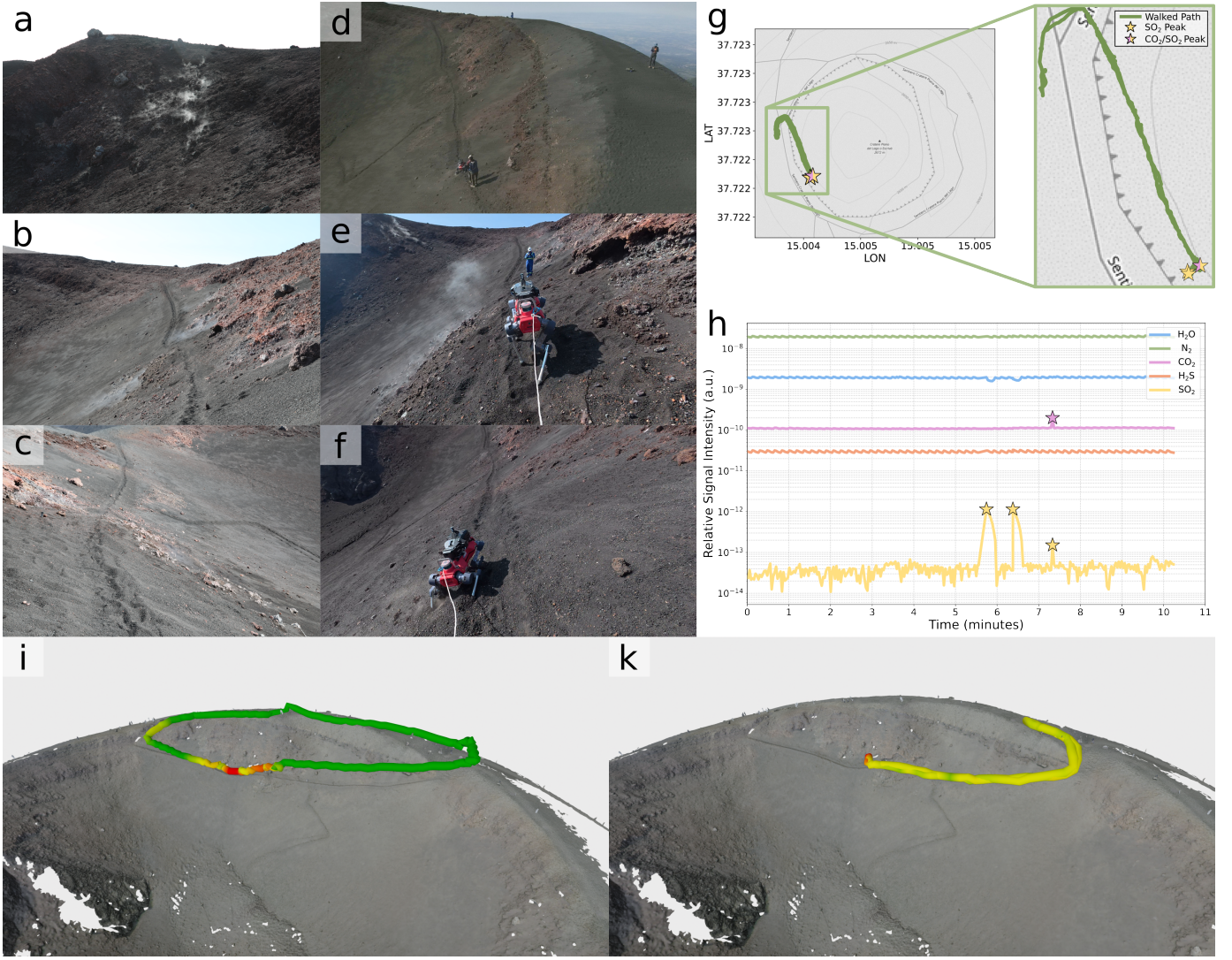


Fig. 7. Overview of the fumarole measurement on Mount Etna. (a-c) Close-up views of fumaroles illustrating typical gas emission features. (d-f) Photographs of the legged robot during operation. (g) Satellite data showing the traversed path with highlighted gas peaks. (h) Time series of measured gas concentrations recorded during the mission, with peaks indicated. (i) Comparison measurement from the miniGAS instrument showing CO_2 concentration. (k) Terrain mesh with the traversed path, color-coded by relative SO_2 concentration.

executed complex paths with minimal operator intervention, confirming the robustness of the navigation stack. Nevertheless, the few required interventions provided valuable insights into the remaining limitations of the system and highlighted directions for future development.

Planning based on global satellite data remains challenging due to its coarse resolution and limited positional accuracy. When following existing trails, the global path accuracy was occasionally affected by misalignments between the OpenStreetMap data and the actual ground path. When planning across open terrain, the operator relied on prior knowledge of large obstacles, such as the untraversable hill in the volcanic desert, that were not visible in satellite imagery. Although such offsets are expected, they can result in infeasible goals for the local planner. An exploration planner could mitigate this issue by finding alternative paths around obstacles; however, for large obstacles such as an extended wall of rocks encountered in Mission 3 (Volcanic Desert), this approach can result

in unnecessarily long or inefficient detours, thereby reducing the robot's overall operational range during long missions. To overcome these limitations, future systems should reduce the information gap between global and local planning. Rather than propagating only discrete waypoints, we propose continuously integrating local observations and feeding them back into the global map to update the current path. This process could be complemented by active perception, where the robot scans its surroundings to evaluate multiple feasible route options before proceeding.

Perception and Localization proved challenging in the volcanic environment. The robot's motion stirred up dust and fine sand, which intermittently degraded both depth camera and LiDAR data. LiDAR-based localization also suffered: scan matching frequently became underconstrained on planar, self-similar slopes, and transient dust returns introduced noise points that increased alignment error and drift. GNSS offered limited support, as satellite coverage was often poor near

crater rims and steep walls, leading to a low-quality signal with high variance and occasional dropouts. Moreover, visual appearance often did not reflect the true soil stability, leading to errors in traversability estimation. A promising solution is adaptive traversability estimation, where the robot refines its terrain model online using feedback from physical interaction.

Locomotion performance during the field tests demonstrated robust operation on volcanic terrain. Over five days of testing across diverse surface types, the robot experienced no falls, highlighting the maturity of current quadruped locomotion policies. Nevertheless, when confronted with even more demanding conditions, such as those encountered during the teleoperated tests, limitations became apparent. Achieving full autonomy capable of reaching fumaroles will likely require reliable traversal of very fine sand on steep slopes – conditions that remain challenging for existing foot designs and locomotion strategies. Improved foot geometries and adaptive contact mechanisms represent a promising approach to increasing stability and traction under these conditions.

VI. CONCLUSION

In this work, we present a robotic system for autonomous measurement of volcanic gases in challenging terrain. The design integrates a mass spectrometer for fast and accurate in situ gas analysis with an autonomy stack that enables long-range traverses across unstructured terrain. Through a series of field trials on Mount Etna, we demonstrated robust navigation across complex volcanic terrain and performed the first successful in situ gas measurements by a ground-based mobile robot on an active volcano, serving as a proof-of-concept. These results establish the proposed system as a viable solution for autonomous volcanic gas analysis, highlighting its potential for advancing field volcanology.

ACKNOWLEDGMENT

The authors would like to thank Simona Scollo, Fabrizia Buongiorno, Gaetano Giudice, Roberto Maugeri, Emilio Pecora, and Luca Merucci from the Istituto Nazionale di Geofisica e Vulcanologia (INGV) for making the Mount Etna field campaign possible, including support with permits and logistical coordination for transport onto the volcano. We further thank Dario Colero Guastella and Giuseppe Sutera from the University of Catania (ROSYs Group) for their valuable on-site support during the Etna experiments.

This work was supported by INFICON Inc., the Luxembourg National Research Fund (Ref. 18990533), and the Swiss National Science Foundation (SNSF) as part of the projects No.200021E_229503 and No.227617.

REFERENCES

- [1] S. K. Brown, S. F. Jenkins, R. S. J. Sparks, H. Odber, and M. R. Auker, “Volcanic fatalities database: analysis of volcanic threat with distance and victim classification,” *Journal of Applied Volcanology*, vol. 6, no. 1, p. 15, 2017.
- [2] J. P. Lockwood, R. W. Hazlett, and S. de la Cruz-Reyna, *Volcanoes: Global Perspectives*. Hoboken, NJ, USA: Wiley Blackwell, 2022.
- [3] V. Acocella, M. Ripepe, E. Rivalta, A. Peltier, F. Galetto, and E. Joseph, “Towards scientific forecasting of magmatic eruptions,” *Nature Reviews Earth & Environment*, vol. 5, no. 1, pp. 5–22, 2024.
- [4] S. A. Carn, “Gas, plume, and thermal monitoring,” in *The Encyclopedia of Volcanoes*, H. Sigurdsson, B. Houghton, S. McNutt, H. Rymer, and J. Stix, Eds. Amsterdam: Elsevier, 2015, pp. 1125–1149.
- [5] J. A. Diaz, C. F. Giese, and W. R. Gentry, “Mass spectrometry for in-situ volcanic gas monitoring,” *TrAC Trends in Analytical Chemistry*, vol. 21, no. 8, pp. 498–514, 2002.
- [6] A. K. Diefenbach, “Special topic—unoccupied aircraft systems,” US Geological Survey, Tech. Rep., 2024.
- [7] M. R. James, B. Carr, F. D’Arcy, A. Diefenbach, H. Dietterich, A. Fornaciari, E. Lev, E. Liu, D. Pieri, M. Rodgers, *et al.*, “Volcanological applications of unoccupied aircraft systems (UAS): Developments, strategies, and future challenges,” *Volcanica*, vol. 3, no. 1, pp. 67–114, 2020.
- [8] G. Muscato, F. Bonaccorso, L. Cantelli, D. Longo, and C. D. Melita, “Volcanic environments: Robots for exploration and measurement,” *IEEE Robotics & Automation Magazine*, vol. 19, no. 1, pp. 40–49, 2012.
- [9] E. Rolland, K. A. R. Grøntved, A. Christensen, M. Watson, and T. Richardson, “Autonomous UAV volcanic plume sampling based on machine vision and path planning,” in *IEEE International Conference on Unmanned Aircraft Systems (ICUAS)*. IEEE, 2024, pp. 1064–1071.
- [10] J. E. Bares and D. S. Wettergreen, “Dante II: Technical description, results, and lessons learned,” *The International Journal of Robotics Research*, vol. 18, no. 7, pp. 621–649, 1999.
- [11] U.S. Geological Survey, “Impacts & mitigation—phones & radios,” https://volcanoes.usgs.gov/volcanic_ash/phones_radios.html, 2015, accessed: 2025-10-07.
- [12] K. Melo, T. Horvat, and A. J. Ijspeert, “Animal robots in the African wilderness: Lessons learned and outlook for field robotics,” *Science Robotics*, vol. 8, no. 85, p. eadd8662, 2023.
- [13] C. G. Wilson, F. Qian, D. J. Jerolmack, S. Roberts, J. Ham, D. Koditschek, and T. F. Shipley, “Spatially and temporally distributed data foraging decisions in disciplinary field science,” *Cognitive Research: Principles and Implications*, vol. 6, no. 1, p. 29, 2021.
- [14] P. Arm, G. Waibel, J. Preisig, T. Tuna, R. Zhou, V. Bickel, G. Ligeza, T. Miki, F. Kehl, H. Kolenbach, *et al.*, “Scientific exploration of challenging planetary analog environments with a team of legged robots,” *Science Robotics*, vol. 8, no. 80, p. eade9548, 2023.
- [15] M. Mattamala, N. Chebrolu, B. Casseau, L. Freiβmuth, J. Frey, T. Tuna, M. Hutter, and M. Fallon, “Autonomous forest inventory with legged robots: System design and field deployment,” 2024.
- [16] J. A. Diaz, D. Pieri, K. Wright, P. Sorensen, R. Kline-Shoder, C. R. Arkin, M. Fladeland, G. Bland, M. F. Buongiorno, C. Ramirez, *et al.*, “Unmanned aerial mass spectrometer systems for in-situ volcanic plume analysis,” *Journal of the American Society for Mass Spectrometry*, vol. 26, no. 2, pp. 292–304, 2015.
- [17] G. Boeing, “Modeling and analyzing urban networks and amenities with OSMnx,” *Geographical Analysis*, 2025.
- [18] J. Nubert, T. Tuna, J. Frey, C. Cadena, K. J. Kuchenbecker, S. Khattak, and M. Hutter, “Holistic fusion: Task- and setup-agnostic robot localization and state estimation with factor graphs,” 2025.
- [19] T. Tuna, J. Nubert, Y. Nava, S. Khattak, and M. Hutter, “X-ICP: Localizability-aware lidar registration for robust localization in extreme environments,” *IEEE Transactions on Robotics*, vol. 40, pp. 452–471, 2023.
- [20] T. Miki, L. Wellhausen, R. Grandia, F. Jenelten, T. Homberger, and M. Hutter, “Elevation mapping for locomotion and navigation using GPU,” in *2022 IEEE/RSJ International Conference on Intelligent Robots and Systems (IROS)*. IEEE, 2022, pp. 2273–2280.
- [21] L. Wellhausen and M. Hutter, “Rough terrain navigation for legged robots using reachability planning and template learning,” in *2021 IEEE/RSJ International Conference on Intelligent Robots and Systems (IROS)*. IEEE, 2021, pp. 6914–6921.
- [22] M. Mattamala, N. Chebrolu, and M. Fallon, “An efficient locally reactive controller for safe navigation in visual teach and repeat missions,” *IEEE Robotics and Automation Letters*, vol. 7, no. 2, pp. 2353–2360, 2022.
- [23] T. Miki, J. Lee, J. Hwangbo, L. Wellhausen, V. Koltun, and M. Hutter, “Learning robust perceptive locomotion for quadrupedal robots in the wild,” *Science Robotics*, vol. 7, no. 62, p. eabk2822, 2022.
- [24] D. R. Olsen and M. A. Goodrich, “Metrics for evaluating human-robot interactions,” in *Proceedings of PERMIS*, vol. 2003. Faculty Publications Gaithersburg, 2003, p. 4.